

Computing thermodynamic observables on noisy quantum computers with chemical accuracy

Spencer T. Stober^{*1}, Stuart M. Harwood¹, Donny Greenberg², Tanvi P. Gujarati³, Sarah Mostame², Sumathy Raman¹, and Dimitar Trenev¹

¹ExxonMobil Corporate Strategic Research, Annandale, NJ 08801, USA

²IBM T.J. Watson Research Center, Yorktown Heights, NY 10598, USA

³IBM Research Almaden, San Jose, CA 95120, USA

Abstract

Quantum computers are a disruptive technology that promise to solve problems that are intractable on conventional computers. The solution of the Schrödinger equation to obtain the energy and electronic configuration of molecules is one such problem because of its exponential scaling with respect to particle number¹. If this problem can be solved, second derivatives of the electronic energy with respect to nuclear position can determine molecular vibrational modes, which can be used to compute thermodynamic observables. Thermodynamic properties of molecules are vital to process engineering, chemistry, astronomy, biology, and other diverse fields. However, to be useful, predicted thermodynamic observables need sufficient accuracy. In chemistry, so called *chemical accuracy* is achieved if the calculated properties lie within ± 1 kcal/mol of experimental reference data. This level of accuracy is often sufficient for most purposes. However, construction of sufficiently accurate derivatives needed to reach chemical accuracy has proven difficult using electronic energy calculations on noisy quantum computers, because of their inherent noise. Here, we report substantial improvements that for the first time have enabled chemical accuracy with respect to predicting thermodynamic properties using a quantum computer. To achieve this, we have developed a noise-tolerant procedure to use energy results from the quantum computer to compute thermodynamic observables. In addition, we developed a new classical optimization procedure, that improves the efficiency and accuracy of the variational quantum eigensolver (VQE) algorithm on quantum devices — compared to the exact solution, error in predicted energy using actual hardware has been reduced by two orders of magnitude compared to the current state-of-the-art technique, using equivalent computing time. Using these techniques on a quantum computer, we computed thermodynamic observables for hydrogen, hydrogen deuteride, deuterium, and their isotopic exchange reaction with chemical accuracy, which would not have been possible without these improvements. We anticipate our improvements will serve as a starting point for predicting thermodynamic observables of more complex systems on noisy quantum computers. The improved efficiency in the VQE algorithm facilitated by the new optimizer may also provide benefits in a broad range of quantum computing problems, such as combinatorial optimization, or other problems that can be cast as eigenvalue problems. Furthermore, introducing the benchmark of chemical accuracy to quantum computing will motivate research into enhancing precision as hardware and algorithms are scaled to larger systems.

^{*}Corresponding author: spencer.t.stober@exxonmobil.com

Main

Calculation of thermodynamic observables from electronic energy calculations typically requires several steps: (i) calculation of the Born-Oppenheimer potential energy surface (BOPES); (ii) determination of intramolecular vibrational modes; and (iii) calculation of the partition function and thermodynamic observables as a function of temperature and pressure. Typically, the first step is the computational bottleneck since it requires solving the Schrödinger equation for a fixed position of nuclear coordinates, a task that quantum computers have the potential to accelerate beyond what is possible using classical computers^{2,3,4}.

By harnessing the quantum nature of matter, quantum computers have been constructed that can manipulate entanglement and superposition of qubits, and thus naturally represent, and operate on, different quantum states. Several advances in algorithms for computational chemistry on quantum computers have enabled noisy quantum computers, with only a few qubits, to approximate solutions to the Schrödinger equation. First, the variational quantum eigensolver (VQE)^{5,6} is a hybrid quantum-classical algorithm that reduces the long coherence times required by the (all-quantum) quantum phase estimation algorithm⁷. The efficiency of VQE has also been improved by using particle/hole mapping of the Hamiltonian, which produces a better starting point for the trial wavefunction⁸. Methods have also been developed that reduce the number of qubits required for electronic structure calculations, like qubit tapering⁹, by eliminating redundant degrees of freedom in the Hamiltonian. In addition, measurement error mitigation can be used to reduce the error in measuring the state of the qubits on a quantum device^{10,11}.

Using combinations of these techniques, noisy quantum computers have been used to compute the BOPES of small molecular systems (step i, above), such as HeH^+ ^{5,12}, H_2 ^{13,6}, and LiH ^{6,14}. Because these systems comprise two atoms, the only molecular degree of freedom in the BOPES is the distance between these atoms. Thus, for diatomic molecules, the BOPES is the electronic energy as a function of interatomic distance. However, these calculations have been too noisy for the determination of rotational and vibrational wavenumbers (step ii, above) using traditional methods, such as constructing the Hessian (a matrix of second-order partial derivatives of electronic energy with respect to nuclear coordinates) by finite differences and finding its eigenvalues and eigenvectors.

To address this problem, we present here two new approaches. First, a new classical optimization procedure for the VQE algorithm was developed. The new algorithm uses Gradient descent, Bootstrapping, Epochs, and adaptive Resampling (GRABER) to improve the precision and efficiency of the VQE algorithm. Given similar numbers of function evaluations on the quantum computer, the mean electronic energy across the dissociation curve of hydrogen deviated from the exact solution by 2.15 kcal/mol for GRABER, compared to 267 kcal/mol for the current state-of-the-art optimizer (simultaneous perturbation stochastic approximation, SPSA). We have also developed a method using a parameterized molecular potential energy function (the Morse potential¹⁵) to ameliorate the noise inherent in single-point energy calculations on noisy quantum computers. Using these methods we have computed a high-accuracy BOPES for hydrogen on a quantum computer using two superconducting transmon qubits¹⁶ (a detailed description of the hardware is in Methods). The BOPES was then used to compute thermodynamic observables, which were compared to experimental data.

The first example reproduces one of the earliest calculations in quantum mechanics, the rotational heat capacity of *ortho*- and *para*- H_2 at low temperatures (*ortho*- and *para*- refer to the nuclear spins pointing in the same or opposite directions, respectively). This seemingly simple calculation stumped early theoreticians working on quantum mechanics (e.g., Einstein, Plank, Nernst, Bohr, Schrödinger) in the 1900's¹⁷. Early theories were unable to account for experimental heat capacity results of hydrogen's isomers until David Dennison and Ralph Fowler described the coupling of nuclear spin with rotational modes in 1927, ushering in modern chemical quantum mechanics¹⁸. The quantum computer calculations presented here agree well with their experimental data.

Next, we computed thermodynamic observables for H_2 , D_2 , and HD . For these calculations, we have achieved chemical accuracy with respect to modern reference data from NIST¹⁹ for the heat capacity of

these molecules, and the enthalpy, entropy, and free energy for their isotopic exchange reaction, $\text{H}_2 + \text{D}_2 \rightleftharpoons 2\text{HD}$.

As mentioned above, the first step in computing thermodynamic observables is generating the BOPES for our system, H_2 . To do this, single-point energy calculations of H_2 were performed on a superconducting transmon quantum device (see Methods – Hardware) at selected bond lengths using the STO-3G²⁰ basis set and a hardware-efficient VQE algorithm⁶. The resulting BOPES was fit to a Morse potential to determine vibrational modes and ameliorate the effect of noise in the calculated BOPES. From this, the translational, rotational, and vibrational partition functions were computed as a function of temperature, and used to compute desired thermodynamic observables. The following describes these steps in detail.

The variational quantum eigensolver

As noted in the introduction, VQE⁵ is a hybrid quantum-classical algorithm that is more applicable to noisy quantum computers of the near future than alternative quantum eigenvalue algorithms such as quantum phase estimation. At its core, VQE is simply a minimization of the expectation value $E_H(\psi) = \langle \psi | H | \psi \rangle$, where H is some given Hamiltonian and ψ is a quantum state. Note that mathematically $E_H(\psi)$ is just the Rayleigh quotient for the Hermitian matrix $H \in \mathbb{C}^{2^n \times 2^n}$ and the unit vector $\psi \in \mathbb{C}^{2^n}$ and one indeed has

$$\min_{\psi \in \mathbb{C}^{2^n}} E_H(\psi) = \min_{\psi \in \mathbb{C}^{2^n}} \langle \psi | H | \psi \rangle = \langle \phi_0 | H | \phi_0 \rangle = \lambda_0,$$

where λ_0 is the smallest eigenvalue of H and ϕ_0 is its corresponding eigenvector.

Leveraging the respective strengths of classical and quantum computers, VQE performs the (classically-expensive or intractable) expectation value evaluations on a quantum device²¹, and uses a classical optimization algorithm to minimize E_H . Furthermore, to make the optimization algorithm classically-tractable, the dimension of the optimization space is reduced by using a parameterized quantum circuit $U : \mathbb{R}^m \rightarrow \mathbb{C}^{2^n \times 2^n}$, as the “ansatz”, which maps the low-dimensional space \mathbb{R}^m to unitary operators $U(\theta)$. The VQE algorithm then becomes a (classical) minimization of the (quantum-evaluated) function $f : \mathbb{R}^m \rightarrow \mathbb{R}$ given by

$$f(\theta) = \langle U(\theta)\psi_0 | H | U(\theta)\psi_0 \rangle.$$

In the above definition, $|\psi_0\rangle$ is some given initial state, which is then modified by the parameterized circuit U . It can simply be the state $|0\rangle$, or some other quantum state (ideally, closer to the eigenstate ϕ_0) that can be efficiently constructed by a state-preparation circuit U_0

$$|\psi_0\rangle = U_0 |0\rangle.$$

It should be noted that by minimizing $f(\theta)$ one computes

$$\tilde{\lambda}_0 = \min_{\theta \in \mathbb{R}^m} f(\theta) = \min_{\theta \in \mathbb{R}^m} \langle U(\theta)\psi_0 | H | U(\theta)\psi_0 \rangle \geq \min_{\psi \in \mathbb{C}^{2^n}} \langle \psi | H | \psi \rangle = \langle \phi_0 | H | \phi_0 \rangle = \lambda_0,$$

and equality in the above equation is only achieved if the eigenstate ϕ_0 has a representation of the form $\phi_0 = U(\theta_0)\psi_0$ for some value θ_0 of the ansatz parameters. This underlines the importance of choosing appropriate ansatz and initial state.

In the results presented here, the variational-form of the ansatz is given by single-qubit R_Y rotations interleaved by a series of two-qubit entangling gates^{6,21}, which are better suited to the current hardware than other chemically-inspired ansätze such as the unitary coupled cluster ansatz²². The initial state $|\psi_0\rangle$ and Hamiltonian used here are in the particle/hole representation and they have been mapped to qubits using parity mapping. More details on the variational form, particle/hole representation and qubit mapping are discussed in Methods.

The VQE classical optimizer

A core part of the VQE is the classical optimization method and related heuristics. For this work, we developed an optimization procedure incorporating GRAdient descent, Bootstrapping, Epochs, and adaptive Resampling (GRABER). At its core, the GRABER procedure is a stochastic gradient descent method, which utilizes advanced starting point information (“bootstrapping”), accommodates a custom step length schedule (“epochs,” to appropriate a term from training neural networks), and adaptively adjusts its estimate of the final energy/objective via resampling. When combined together, bootstrapping, adaptively resampling the energy, and the specific step length schedule that we employ enable our efficient and robust calculation of the electronic energies required for the BOPES. The details are discussed below.

The GRABER procedure is based on stochastic gradient descent method (SGD) with momentum*. Gradients are obtained using the parameter shift rule²³. Along with evaluation of the objective/energy estimate at the current parameter point, this makes the cost per iteration of the SGD method $2n_p + 1$ energy evaluations, where n_p is the number of ansatz parameters. This cost is justified as “full” gradient information leads to quicker decrease of the energy. Step lengths decrease to zero with an asymptotic behavior like $1/k$ (where k is the iteration count); this is consistent with most convergence theories²⁴. The specific step length schedule is to use a step length equal to 1 for the first ten iterations, then decrease it by setting it to $1/(k - 10)$, for $k > 10$.

An adaptive termination condition is used. A window of energy estimates from previous iterations is maintained, and the method monitors convergence to a (region near a) stationary point when the change in the windowed average of objective values is less than some tolerance. In the experiments, we take this tolerance equal to 10^{-3} Hartree. This is a heuristic, with no guarantee of convergence in the presence of noise; however, using a window length of four iterations, we see robust performance of the optimizer (i.e., the optimization method converges and avoids hitting an iteration limit).

When the VQE terminates, we have ansatz parameters corresponding to a wavefunction whose energy we need to estimate. Certainly we have evaluated an estimate as part of the optimization procedure; however, depending on the current position on the potential energy surface and what the nuclear coordinates are, this estimate may not be sufficiently accurate. Consequently, one can use the individual circuit shots to estimate a variance σ^2 for the energy estimate following §V.A of Kandala et al.⁶ If we were to repeat the energy estimation N times and take the average, this new estimator would have variance σ^2/N . Consequently, we can ensure that the standard deviation is less than or equal to ϵ by taking $N = \lceil \sigma^2/\epsilon^2 \rceil$ (where $\lceil \cdot \rceil$ is the smallest integer greater than the argument); assuming normality of this estimator, this gives a high probability ($> 68\%$) that the energy estimate is within ϵ of the real value (see Methods – Operator expectation and variance). Again, since the Hamiltonian and thus the estimator and its variance depend on the internuclear distance, so does N , and so the number of repeated samples adapts depending on the location on the BOPES (we refer to this as adaptive resampling). In the experiments, $\epsilon = 10^{-3}$ Ha.

The overall goal is to calculate the electronic energy as a function of internuclear distance in order to obtain the BOPES. Since we expect that the electronic energy landscapes, as a function of the ansatz parameters, at two nearby internuclear distances are similar, we can make the overall calculation of the energies more efficient and consistent by “bootstrapping” the classical optimization at each point along the curve/surface. Specifically, since the ansatz begins with the Hartree-Fock state (in particle/hole representation), which is a reasonable approximation of the state at smaller internuclear distances, we begin the calculation of the electronic energies at the smallest internuclear distance of interest. After the VQE finishes, we have a set of optimal ansatz parameters. Moving to the next smallest internuclear distance, we can use these optimal ansatz parameters as a warm start for the initial point given to the SGD method.

*The specific update is

$$\begin{aligned} m^k &= (1 - \mu)g^k + \mu m^{k-1}, \\ \theta^{k+1} &= \theta^k - \gamma^k m^k \end{aligned}$$

where $m^0 = 0$, $\mu \in [0, 1)$ is the momentum parameter, γ^k is the step length, and g^k is the current gradient estimate. For $\mu = 0$, this reduces to standard SGD. In our experiments, we take $\mu = 0.5$.

In practice, these parameter values are nearly optimal for the new point on the potential energy surface. Combined with the adaptive termination conditions, we can save many iterations of the SGD method. After calculating the whole curve, we repeat this procedure, starting again from the smallest internuclear distance with new random initial ansatz parameters. With three such independent passes, we can throw out outliers at any point along the curve.

Bootstrapping, adaptively resampling the energy, and the specific step length schedule are techniques used in various forms in previous studies employing quantum hardware^{5,6,12,14,25,26}. We believe combining these techniques together enable our efficient and robust calculation of the electronic energies required for the potential energy surface. In Figure 1, we use classical simulations (including modeled hardware noise) of

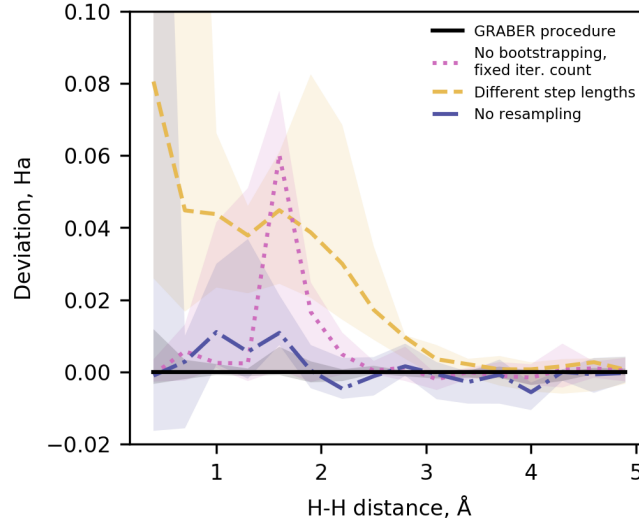


Figure 1: Effects of components of classical optimization procedure. The data represents five VQE solutions at each internuclear distance; the lines are the median, while the shaded regions show the variation (minimum to maximum) over these solutions. We plot deviation of the VQE solutions from a baseline (the GRABER method) at various H-H internuclear distances. “GRABER procedure” represents classical simulation results of our quantum experiment (VQE using STO-3G and particle-hole transform; the main difference is that fewer shots – 1024 – are used in the simulation here). Its median solution forms the baseline that we compare against. “No bootstrapping, fixed iter. count” shows the effect of using a fixed number of iterations (here, 20 iterations) rather than adaptive termination, as well as ignoring warm-start information. “Different step lengths” shows the effect of using a step length schedule of $1/k$. “No resampling” shows the effect of not repeating the energy estimation and averaging.

our quantum experiments to illustrate the contributions of each aspect of the GRABER procedure. We note that these simulations of the hardware, which include noise, accurately represent the experiments on actual hardware (Figure 2, shows this). In the figure, the proposed GRABER optimization procedure corresponds to the “GRABER procedure” data. The effects of leaving out various components, like bootstrapping, resampling, and the specific step length schedule, can be seen. In general, omitting any one of these components leads to either a worse (higher) energy calculation somewhere in the potential energy curve, or greater variation across repeated experiments. For instance, “Different step lengths” shows the effect of using a step length schedule of $1/k$, which tends to get trapped in local minima. The effect of adaptive termination is mostly to improve computational time, and is most apparent when it is combined with bootstrapping. In the GRABER procedure experiments, the most number of iterations required for any data point is 20. Fixing the number of iterations to 20 and ignoring warm-start information to obtain the “No bootstrapping, fixed iter. count” results takes about two times longer compared to the GRABER method. Furthermore, even with this extra calculation time, consistent results are not guaranteed, evident

from the large peak in the variation near 1.6\AA . Only ignoring resampling gives the closest results to the GRABER method; however the variation can be quite large. The maximum value at 0.4\AA is off the scale of the figure, at 0.3Ha .

We note that these techniques may be used to improve other classical optimization methods. Indeed, in the following sections, we will compare against results obtained using the simultaneous perturbation stochastic approximation (SPSA) algorithm in place of GRABER. In these results, we also use bootstrapping and adaptive resampling in the same way as described above. However, they are less effective than when employed in the overall GRABER procedure.

Computing thermodynamic observables

As mentioned above, computing thermodynamic observables begins with single point energy calculations. In this case, we use the quantum computer to compute the BOPES, which is simply the electronic energy as a function of bond length. Since the Born-Oppenheimer approximation assumes stationary nuclei, and the charge of the nuclei for H_2 , D_2 , and HD are identical, their BOPESs will also be identical and need only be computed once (their nuclear mass is taken into account when calculating the partition function). The STO-3G basis set with two spin orbitals, the minimum necessary to describe H_2 , was used with the VQE algorithm. This is similar to performing a classical FCI/STO-3G calculation since the VQE algorithm attempts to find the lowest eigenvalue of the complete Hamiltonian, which is the “Full Configuration Interaction” solution to the electronic Schrödinger equation. For this reason, most of the figures compare the quantum computer calculation, with an FCI/STO-3G calculation on a classical computer — if the quantum computer calculation (with the STO-3G basis set) is perfect, the results should coincide exactly with the FCI/STO-3G classical calculation [†].

Figure 2 shows the BOPES for H_2 computed using the quantum computer and the GRABER or SPSA classical optimizers. Compared to the FCI exact solution, the GRABER optimizer exhibits a mean deviation (across the entire dissociation curve) of 2.15 kcal/mol (max error 5.68 kcal/mol), compared to the SPSA optimizer that had a mean deviation of 267 kcal/mol (max error 402 kcal/mol). In this comparison, we have used roughly the same number of VQE evaluations per point and three points at each bond length. For the SPSA results, we use data obtained from simulations of the quantum hardware with noise, because the long convergence time of the SPSA algorithm made performing these calculations on the actual hardware prohibitive. Note that we would also not expect convergence of SPSA in actual hardware since convergence in the simulation was not achieved. In the figure, we compare results for GRABER using both simulations and actual quantum hardware to show that our simulation protocol is capable of accurately modeling the hardware. The next step in computing thermodynamic observables is typically construction of the Hessian matrix by finite differences, using the quantum harmonic oscillator (QHO) approximation, based on computed single point energies close to the equilibrium bond length. The eigenvalues of the Hessian matrix can then be used to determine the vibrational energy levels. Despite the good agreement between the VQE calculations using GRABER and the FCI/STO-3G calculation, the noise in the quantum computer makes a finite difference-based approach or harmonic fits of the data problematic. In Figure 2 it is clear that fitting a harmonic potential [‡] using the SPSA optimizer produces a fit that differs substantially from the FCI harmonic fit. The GRABER-based harmonic potential fit is much better, but it still diverges from FCI harmonic fit. To achieve the maximum possible accuracy in predicting thermodynamic observables, the potential energy surface used must coincide with the exact solution to the greatest extent possible.

To mitigate this issue, the Morse potential is used as a parameterized potential energy surface (PES) so that the entire dissociation curve can be used to fit the parameters, thus reducing the effect of noise from any one single point energy. The Morse potential is shown in equation 1 where $V(r)$ is the potential energy, which is a function of the interatomic distance, r . The parameters are potential energy well depth,

[†]FCI calculations were performed on a classical computer using the Psi4 software package ²⁷.

[‡]The harmonic potential is $V_{\text{harm}}(r) = \frac{1}{2}kr^2$ where r is the bond length, and k is a spring constant.

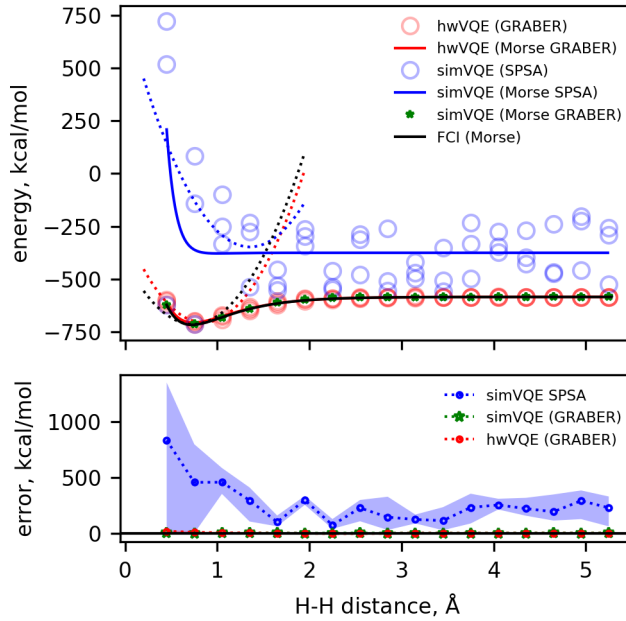


Figure 2: **Top panel:** red circles are single point energy calculations run on quantum hardware using the GRABER classical optimizer. Green stars are calculations that are identical conditions to the red circles, except a hardware simulator (with simulated noise) was used. This demonstrates that the simulated data agree with the actual hardware results. Blue circles are single point energy calculations determined using simulations (with noise) of quantum hardware using the SPSA classical optimizer. Red and blue lines represent Morse (solid line) or QHO (dotted line) PES fits of the calculated single-point energies in corresponding colors. The black lines are the Morse (solid) or harmonic (dotted) potential fits to FCI/STO-3G data from a classical computation, every 0.01 Å from 0.45 to 5.3 Å. **Bottom panel:** error relative to the exact (FCI/STO-3G) solution for the data shown in the top panel. The mean of the three replicates at each distance is indicated by the line and markers. The shaded region shows the range of the replicates.

D_e , the width of the potential energy well, α , which is related to the force constant between the atoms, and the equilibrium bond length r_0 .

$$V(r) = D_e(1 - e^{-\alpha(r-r_0)})^2 \quad (1)$$

Besides noise mitigation, the Morse potential also has several other advantages compared to the finite difference method. The finite difference method typically employs the QHO approximation, which does not accurately capture the uneven spacing of vibrational energy levels or the anharmonicity present in real molecules, which is accounted for in the Morse potential. The Morse potential also has a defined dissociation energy (related to D_e), which will be important later. Importantly, the Morse potential also has analytical solutions for the vibrational energy levels (equation 2), which facilitates calculation of the vibrational partition function, a necessary next step in calculating thermodynamic properties of molecules.

$$\epsilon_n = h\nu_0(n + 1/2) - \frac{[h\nu_0(n + 1/2)]^2}{4D_e}, n = 0, 1, 2, \dots, n_{max} \quad (2)$$

Here, ϵ_n is the vibrational energy at energy level n . h is Plank’s constant, α and D_e are parameters from the Morse potential. ν_0 is the fundamental vibrational frequency, which is related to the reduced mass,

m_R , and parameters of the Morse potential by equation 3.

$$\nu_0 = \frac{\alpha}{2\pi} \sqrt{\frac{2D_e}{m_R}} \quad (3)$$

The summation in the energy levels is usually computed until the dissociation energy, $E_{diss} = D_e - \epsilon_{n,(n=0)}$ is reached. Therefore the maximum value of n is

$$n_{max} = \left\lfloor \frac{2D_e - h\nu_0}{h\nu_0} \right\rfloor, \quad (4)$$

where $\lfloor \cdot \rfloor$ is the largest integer smaller than the argument. Given this method for calculation of the vibrational energy levels, the partition functions can be computed. Note that in the QHO approximation, the dissociation energy is estimated from the dissociation curve (it is not a fit parameter like the Morse potential).

The partition function for a molecule is the product of contributions from translational, rotational, vibrational, electronic, and nuclear degrees of freedom, as shown in equation 5, where V and T are volume and temperature, respectively.

$$q(V, T) = q_{translation} q_{rotation} q_{vibration} q_{electronic} q_{nuclear} \quad (5)$$

We assume the electronic and nuclear parts of the molecular partition function are unity since nuclear and electronic excited states are not accessible for our system at reasonable temperatures.

Once $q(V, T)$ has been determined as a function of temperature, the internal energy and Helmholtz (U and A , respectively), can be obtained via differentiation (holding V constant)

$$U = k_B T^2 \left. \frac{\partial \ln q(V, T)}{\partial T} \right|_V, \quad (6)$$

$$A = -k_B T \ln(q(V, T)), \quad (7)$$

where k_B is the Boltzmann constant. Once U and A are determined, other relevant thermodynamic observables can be calculated easily^{28 §}.

Next, the procedure to calculate each contribution to the molecular partition function is described. The translational partition function can be calculated classically

$$q_{translation} = \left(\frac{2\pi m k_B T}{h^2} \right)^{3/2} V, \quad (8)$$

where volume, V , is obtained from the ideal gas law, $V = k_B T/P$.

The vibrational partition function is computed from the Boltzmann summation of the vibrational energy levels from the PES (ϵ_n in equation 2)

$$q_{vibrational} = \sum_n^{n_{max}} e^{-\epsilon_n/k_B T}. \quad (9)$$

In the QHO approximation, the levels are evenly spaced, which is a source of error, since in actuality they have decreasing spacing (which is exhibited by the Morse potential). Also, as mentioned earlier, the dissociation energy is estimated for the QHO PES to truncate this summation.

The rotational partition function for HD, a heteronuclear diatomic molecule, is calculated according to equation 10.

$$q_{rotational}^{equib}(T) = \sum_{J=0}^{J_{max}} (2J+1) e^{-\Theta_r J(J+1)/T} \quad (10)$$

[§]Herein, we derive the discussed thermodynamic functions as follows $S = (U - A)/T$; $H = U + PV$, where $PV = k_B T$; $G = H - TS$; $C_v = \left. \frac{\partial U}{\partial T} \right|_{N,V}$; and $C_p = \left. \frac{\partial H}{\partial T} \right|_{N,P}$;

Here, J is the rotational mode (an integer), and the rotational temperature, Θ_r , is

$$\Theta_r = \frac{\hbar^2}{2I_M k_B}. \quad (11)$$

The energy of each rotational mode, ϵ_{rot} is

$$\epsilon_{rot} = \frac{\hbar^2}{2I_M} J(J+1), \quad (12)$$

where \hbar is the reduced Plank's constant and I_M is the moment of inertia at the equilibrium bond length. We can calculate the maximum value for J by limiting the rotational energy level to be less than the dissociation energy:

$$J_{max} = \left\lfloor \frac{\sqrt{\hbar^2 + 8\epsilon_{rot} I_M} - \hbar}{2\hbar} \right\rfloor, \quad \epsilon_{rot} = E_{diss}. \quad (13)$$

Note that the rotational partition function depends on the PES via the dissociation energy (limiting the the number of energy levels), and the equilibrium bond length (in the moment of inertia). The method of obtaining the dissociation energy is mentioned above; the equilibrium bond length can be obtained from the PES fit for both the QHO and Morse potentials (i.e., it is the bond length at the minimum energy).

However, the rotational partition function of homonuclear diatomic molecules is different from heteronuclear molecules, and was a challenge for early quantum mechanics until coupling of nuclear spin with rotational modes was understood. A detailed explanation of this phenomenon is provided by McQuarrie²⁸; we provide a brief summary here. In essence, since each nucleus of a homonuclear diatomic molecule is an identical particle, if the nuclei are interchanged, the total wavefunction must be symmetric for bosons (integer nuclear spin) or antisymmetric for fermions (half-integer nuclear spin). H_2 has half-integer nuclear spin (D_2 has integer nuclear spin) so the nuclei can have parallel spins or opposite spins, called ortho- H_2 and para- H_2 , respectively. To maintain the correct antisymmetry of the wavefunction for both types of H_2 , the rotational modes that are even couple to opposite nuclear spins (para- H_2), and odd modes couple to parallel nuclear spins (ortho- H_2). The sum of these two terms is the partition function for the equilibrium mixture of ortho- H_2 and para- H_2 , shown in equation 15[¶], where I is the nuclear spin.

$$\begin{aligned} q_{rot-nuc}^{equib-H_2}(T) &= q_{rot-nuc}^{para-H_2}(T) + q_{rot-nuc}^{ortho-H_2}(T) \\ &= I(2I+1) \sum_{J \text{ even}}^{J_{max}} (2J+1)e^{-\Theta_r J(J+1)/T} + (I+1)(2I+1) \sum_{J \text{ odd}}^{J_{max}} (2J+1)e^{-\Theta_r J(J+1)/T} \\ &= 1 \sum_{J \text{ even}}^{J_{max}} (2J+1)e^{-\Theta_r J(J+1)/T} + 3 \sum_{J \text{ odd}}^{J_{max}} (2J+1)e^{-\Theta_r J(J+1)/T} \end{aligned} \quad (15)$$

A consequence of the functional form of the rotational partition function for homonuclear diatomic molecules is that the ratio of para- H_2 : ortho- H_2 approaches 1 : 3 as temperature increases, according to the relation

$$x_{para-H_2} = \frac{q_{rot-nuc}^{para-H_2}(T)}{q_{rot-nuc}^{equib-H_2}(T)}, \quad (16)$$

where x_{para-H_2} is the mass fraction of para- H_2 . In equation 15 this 1 : 3 ratio is reflected in the coefficients of the summations in the third line, which result from substituting the nuclear spin of H_2 ($I = 1/2$) into the second line.

[¶]A similar argument explains the partition function for D_2 , (equation 14) except rotational modes that are odd couple to opposite nuclear spins (para- D_2), and even modes couple to parallel nuclear spins (ortho- D_2)

$$q_{rot-nuc, I=\text{integer}}^{equib}(T) = I(2I+1) \sum_{J \text{ odd}}^{J_{max}} (2J+1)e^{-\Theta_r J(J+1)/T} + (I+1)(2I+1) \sum_{J \text{ even}}^{J_{max}} (2J+1)e^{-\Theta_r J(J+1)/T} \quad (14)$$

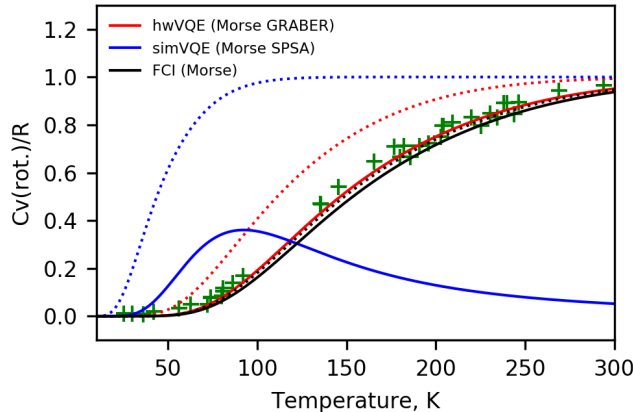


Figure 3: The constant volume rotational heat capacity computed using partition functions derived from PES fits of single point energy calculations using the Morse (solid lines) or QHO (dotted lines) potentials. Red, blue, and black lines represent the GRABER, SPSA, or exact FCI solutions, respectively. GRABER data is from hardware calculations and SPSA data is a simulation of the hardware including noise. Green crosses represent experimental data measured on normal H_2 ^{29,30}.

Figure 3 compares several methods to determine the rotational heat capacity of normal- H_2 compared with experimental data. The rotational heat capacity is simply the heat capacity computed using only the rotational part of the partition function[‡]. The FCI calculations show that, for this case, using the Morse potential or QHO potential to compute the rotational partition function and heat capacity are nearly equivalent. However, using quantum hardware (or hardware simulator) results in noise-induced deviations from the exact solution for the PES fit (see also Figure 2). This error propagates to the partition function and resulting thermodynamic calculations, causing the deviation from the experimental data and FCI solutions shown in Figure 3. With SPSA, this error is large for both the Morse and QHO PES. However, the improved single point energy calculations using the GRABER optimizer result in a much closer fit, especially for the Morse potential, which matches experimental data nearly perfectly (and also coincides with the exact FCI solution).

Figure 4 shows the constant pressure heat capacity (C_p) as a function of temperature for H_2 , D_2 , and HD, calculated by using the methodology described, above. Experimental data are from NIST¹⁹. Here, we have taken into account the nuclear spin to rotational coupling for H_2 , D_2 . This is not necessary for HD since the nuclei are not identical.

In the low temperature regime the experimental C_p data is best predicted by the hwVQE (Morse GRABER) method (n.b., the red line in Figure 4 representing this calculation overlaps the black FCI (Morse) line almost perfectly, which somewhat obscures it).

In the high temperature limit, the smearing of quantized energy levels into a continuum leads to a convergence in predicted C_p for the Morse and QHO PES methods — except for the Morse-SPSA case, which is due to a poor fit due to noisy SPSA data. Also in the high temperature regime, it is apparent that the predicted C_p underestimates the experimentally determined values. To determine if this underestimation was the result of the minimal basis set used for most calculations (STO-3G), single point energies were computed every 0.01 Å from 0.45 to 5.3 Å using FCI/6-311G(3df,2pd). Based on a Morse PES fit of these data, C_p was computed — this is the green line in Figure 4. From this, it is clear that

[‡]For normal- H_2 , the mixture is not at equilibrium and its rotational partition function³¹ is therefore

$$q_{\text{rot-nuc}}^{\text{norm-H}_2}(T) = (q_{\text{rot-nuc}}^{\text{para-H}_2}(T))^{x_{\text{para}}} (q_{\text{rot-nuc}}^{\text{ortho-H}_2}(T))^{x_{\text{ortho}}}. \quad (17)$$

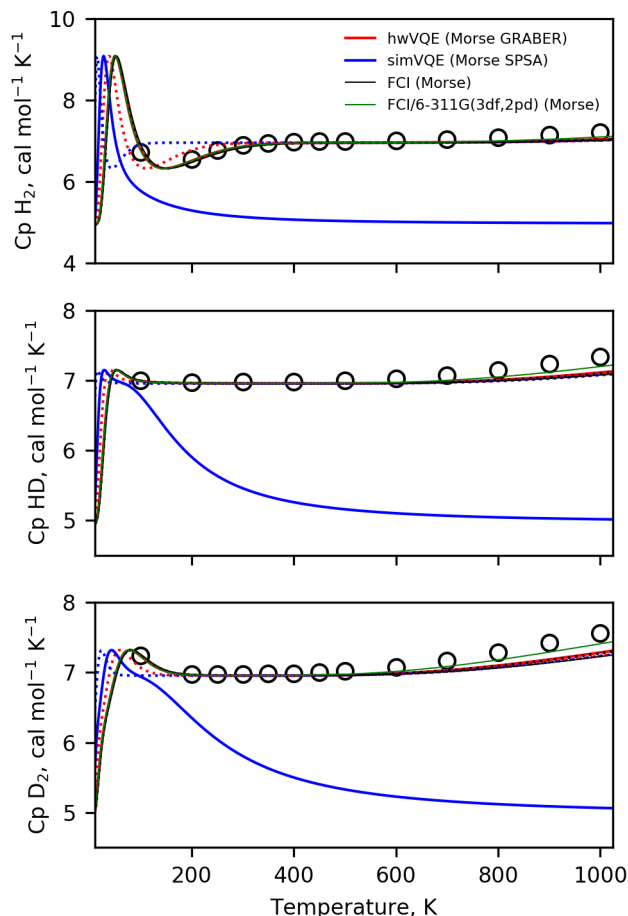


Figure 4: The top, middle, and bottom panels show the calculated and experimental constant pressure heat capacity (C_p) for H_2 , HD , and D_2 , respectively. Circles are experimental data from NIST¹⁹. Red, blue, and black lines represent the GRABER, SPSA, or exact FCI solutions, respectively. Calculations using the Morse are solid lines, the QHO potential uses dotted lines. GRABER data is from hardware calculations (hw prefix) and SPSA data is a simulation (sim prefix) of the hardware including noise. Also included in green is the calculated C_p using a Morse PES from FCI/6-311G(3df,2pd) single point energies.

the FCI/6-311G(3df,2pd)-based method still does not capture the heat capacity perfectly, although it is an improvement compared to FCI/STO-3G. In fact, this is a result of the imperfect description of the real PES by the Morse potential.

Figure 5 shows the deviation of the Morse potential fit of single-point energies from the single-point calculations themselves. Compared to FCI/STO-3G (two spin orbitals), FCI/6-311G(3df,2pd) (28 spin orbitals) exhibits less error in the Morse fit compared to the single point energies, which translates into a noticeable improvement in predicted C_p in the high temperature regime. However, compared to FCI/6-311G(3df,2pd), increasing the size of the basis set to FCI/aug-cc-pVQZ (92 spin orbitals) leads to nearly identical error with respect to the Morse fit of the single point energies.

These results show that as the size of the basis set increases, there is a limit beyond which the Morse potential fit does not improve; i.e., the functional form of the Morse potential itself is not capable of describing the real PES perfectly. This result is not surprising since development of potentials with additional parameters to improve this disagreement is an active area of research, although they don't usually benefit from having a closed form for their eigenenergies. More general regression methods like

Gaussian processes or splines would also suffer from difficult to obtain eigenenergies.

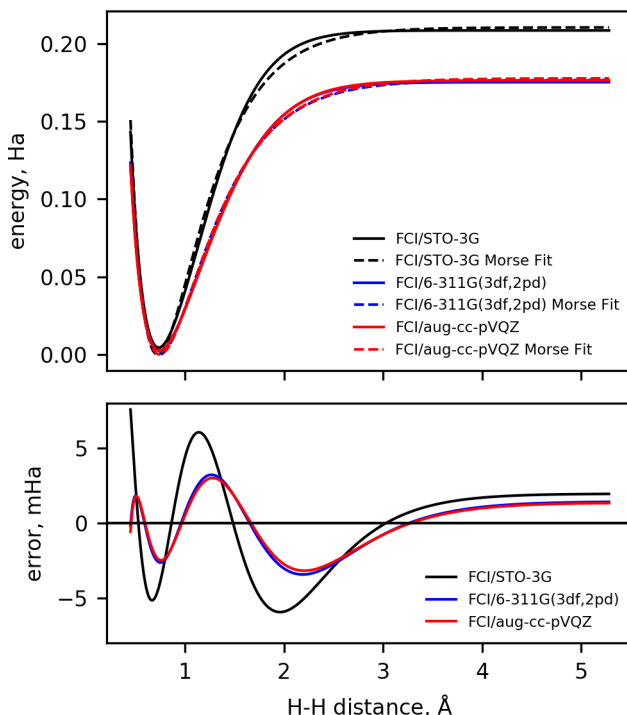


Figure 5: **Top panel:** Comparison of single point energy calculations with Morse PES fits of the same data. Single point energy calculations are calculated classically, every 0.01 Å from 0.45 to 5.3 Å (solid lines). The Morse PES fit of these data are shown as dashed lines. **Bottom panel:** Error in the fit of the Morse PES compared to single point energies. Here, error as a function of H-H distance is computed as $Error = Energy_{Morse} - Energy_{Single\ point}$.

Next, thermodynamic observables for the isotopic exchange reaction, $H_2 + D_2 \rightleftharpoons 2HD$ were determined. To obtain ΔH_{rxn} , ΔS_{rxn} , and ΔG_{rxn} , the thermodynamic observables for each individual species are determined (by the methods described previously). Then the reaction thermodynamics can be calculated by $\Delta M_{rxn} = M_{products} - M_{reactants}$, where M is a thermodynamic observable — H , S , or G , in this case. Figure 6 shows ΔH_{rxn} , ΔS_{rxn} , and ΔG_{rxn} , as a function of temperature.

ΔG_{rxn} is predicted equally well by all methods. However, this is because $\Delta G_{rxn} = \Delta H_{rxn} - T\Delta S_{rxn}$ and the magnitude of ΔH_{rxn} is very small compared to the $T\Delta S_{rxn}$ term. Therefore, this quantity is dominated by the contribution of temperature, which is not a function of our calculations.

For ΔS_{rxn} , all methods converge in the high temperature limit for reasons previously discussed. At low temperatures, both the Morse and QHO PES calculations with the GRABER optimizer agree with experimental data to within about 0.001 kcal/mol. Although the calculations using combinations of Morse-SPSA and QHO-GRABER appear to be a better match to the data, this must be disregarded since in these cases the predictions do not coincide with the exact FCI calculations using the Morse or QHO PES, which implies that any perceived increased accuracy is due to coincidence.

For ΔH_{rxn} despite an offset of about 0.6 kcal/mol compared to NIST data, the Morse potential calculations with the GRABER optimizer best capture the trend of the data (since the offset is small, and relatively constant across the temperature range). Like for ΔS_{rxn} , the results for the SPSA optimizer and QHO PES should be considered coincidence, despite their sometimes close approach to the experimental data.

Although the peak present in ΔH_{rxn} and ΔS_{rxn} at about 150 K is not reflected in the NIST data, this is likely due to the absence of an experimental data point at this temperature. That the calculation captured

the rotational heat capacity of norm- H_2 in this temperature range (see Figure 3) underpins our assertion that the peak in ΔH_{rxn} is real, and is due to the coupling of nuclear and rotational degrees of freedom, as discussed previously. Nonetheless, it is apparent that chemical accuracy was achieved for all predictions based on inspection of the Figure 6 y-axis scale with respect to the ± 1 kcal/mol limits of this benchmark.

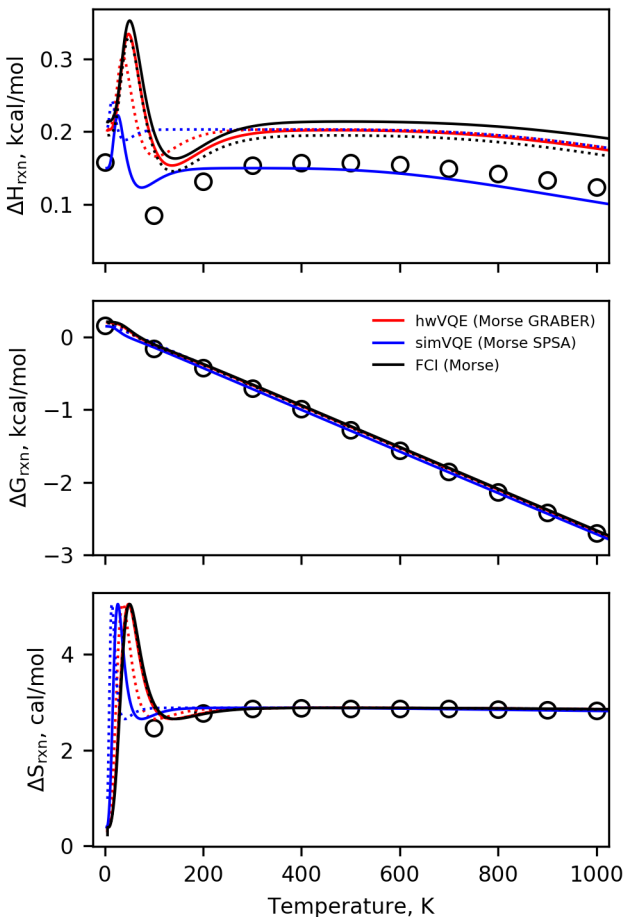


Figure 6: The top, middle, and bottom panels are ΔH_{rxn} , ΔS_{rxn} , and ΔG_{rxn} , respectively. Circles are experimental data from NIST¹⁹. Red, blue, and black lines represent the GRABER, SPSA, or exact FCI solutions, respectively. Calculations using the Morse are solid lines, the QHO potential uses dotted lines. GRABER data is from hardware calculations (hw prefix) and SPSA data is a simulation (sim prefix) of the hardware including noise.

These findings demonstrate that, compared to experimental results, the techniques described herein enable chemically accurate thermodynamic calculations using noisy quantum computers for the $\text{H}_2 + \text{D}_2 \rightleftharpoons 2\text{HD}$ reaction, its components, and their nuclear spin isomers. We anticipate that the method of potential fitting will serve as a starting point to enable accurate thermodynamic predictions using early quantum devices, although additional potential functions will be necessary to capture bending and torsional rotations in larger molecules. The GRABER classical optimizer substantially improves the efficiency of the VQE algorithm, which will have impact in computational chemistry but also in all fields where systems can be cast as eigenvalue problems. Finally, by introducing the benchmark of chemical accuracy, we hope to motivate increases in qubit coherence time and measurement fidelity as larger, more interconnected, quantum computers are constructed and used for computational chemistry.

Methods

Detailed procedure

To provide context for how thermodynamic observables are calculated on a quantum computer, the following provides the step-by-step procedure.

1. Selection of the basis set and list of bond lengths for the H₂ potential energy surface.
2. For each bond length, an initial state, $|\psi_0\rangle$, is constructed using the Hartree-Fock Hamiltonian and the selected basis set. This was done using PySCF³², a quantum chemistry code.
3. This initial state and Hamiltonian is transformed from the Hartree-Fock representation to a particle/hole representation⁸.
4. This Hamiltonian is then mapped to a qubit Hamiltonian using parity mapping^{33,34}. For H₂ and the STO-3G basis set, this requires 2 qubits.
5. Qubit tapering may be used to find symmetries in this Hamiltonian, which may reduce the number of qubits required. Although we have not taken this step, it is described since it will be vital to enable simulation of larger molecules or basis sets.
6. The VQE algorithm is applied using the particle/hole qubit Hamiltonian and a parameterized quantum circuit consisting of the particle/hole representation of the initial state, followed by an R_Y ansatz with depth one^{6,21}. This consists of an R_Y gate on each qubit, followed by entanglement using controlled- Z gates between each pair of qubits, and a final R_Y gate for each qubit. The rotation angle of each R_Y gate is tunable, resulting in two parameters for each qubit that can be optimized in the VQE algorithm. During each circuit execution and measurement, measurement error mitigation has been applied to improve the precision of results. The output of the VQE procedure is the single-point energy at the selected bond length.
7. The set of these bond lengths and energies is then used to fit the parameters of the Morse potential.
8. Using these parameters, the partition function is computed as a function of temperature, and the result is used to compute thermodynamic observables.

The particle/hole transformation

Variational quantum algorithms for quantum chemistry require the preparation of suitable trial wavefunctions. The particle/hole transformation in this context provides a better reference trial wavefunction and improves realization of the VQE algorithm⁸. The method is based on transforming the electronic Hamiltonian in the second quantization into the particle/hole picture where the state of the molecular system of interest is parameterized to efficiently explore the sector of the molecular Fock space that contains the desired solution. The electronic Hamiltonian in the particle/hole picture is given by

$$H^{p/h} = E_{\text{HF}} + \sum_{rs} \langle r | F | s \rangle N_b \left[a_r^\dagger a_s \right] + \frac{1}{2} \sum_{srtu} \langle rs | g | tu \rangle N_b \left[a_r^\dagger a_s^\dagger a_u a_t \right] \quad (18)$$

with $\langle r | F | s \rangle$ being the Fock matrix $\langle r | F | s \rangle = \langle r | h | s \rangle + \sum_i (\langle ri | g | si \rangle - \langle ri | g | is \rangle)$, and

$$E_{\text{HF}} = \sum_i \langle i | h | i \rangle + 1/2 \sum_{ij} (\langle ij | g | ij \rangle - \langle ij | g | ji \rangle) \quad (19)$$

where h and g are the one- and two-electron integral operators, respectively. The normal ordering operator N_b acts on the particle/hole operators, see⁸ for more details.

Qubit tapering

The particle/hole Hamiltonian requires mapping to a qubit Hamiltonian for implementation of the VQE procedure on a quantum computer. For the current near-term quantum devices, the number of physical qubits remains a valuable resource. It is imperative that all possible steps which can reduce the number of qubits required for mapping the problem Hamiltonian onto the quantum hardware must be taken. Here, we describe how to use qubit tapering⁹ to reduce the number of qubits required for this calculation. In this case, the qubit requirements for simulating an H_2 molecule may be reduced from two qubits (STO-3G basis) to only one qubit. While we have not used it in the present calculations, it will be a vital step for simulating larger molecules or larger basis sets.

It is a well-known fact that standard molecular electronic Hamiltonians conserve the number of particles with fixed spin orientations. This implies that the problem can be effectively described in a subspace of the full Hilbert space with the right number of spin-up and spin-down particles. This reduction in the required Hilbert space is a result of the spin-particle conservation symmetry of the Hamiltonian. Apart from these symmetries, certain molecules also exhibit spatial or geometric symmetries under the operations described by reflections or rotations. On mapping the second quantized representation of the fermionic molecular Hamiltonian to a qubit Hamiltonian by using the well-known encodings like Jordan-Wigner³⁵ or its variants such as parity encoding^{33,34} and binary tree encodings³³, the symmetries corresponding to spin-particle number conservation and some geometric symmetries are captured by the \mathbb{Z}_2 symmetries of the qubit Hamiltonian^{9,36}. The qubit tapering procedure provides us with a systematic way of finding multiple \mathbb{Z}_2 symmetries in the qubit Hamiltonian and transforming this Hamiltonian such that one qubit for each \mathbb{Z}_2 symmetry can be removed from the description. This is an exact procedure and hence the energy spectrum obtained from the original Hamiltonian and the tapered Hamiltonian is identical. For the mathematical and algorithmic details of how the qubit tapering procedure works please refer to reference⁹.

The qubit tapering procedure not only helps reduce the required qubit count, but it also reduces the depth of the heuristic ansatz required to solve the problem using VQE. The reduced depth of the quantum circuit in turn helps in decreasing the errors incurred due to finite coherence times of the qubits on the near-term devices.

Routines available in Qiskit Aqua¹¹ can perform qubit tapering on the H_2 Hamiltonian.

Operator expectation and variance

The adaptive resampling used in GRABER depends on the variance of the estimator of the energy, \hat{E} . The Hamiltonian of interest H is implemented as $H = \sum_{\alpha=1}^{n_o} h_{\alpha} P_{\alpha}$; thus the true energy $\langle H \rangle$ is estimated by

$$\langle \widehat{H} \rangle = \sum_{\alpha=1}^{n_o} h_{\alpha} \langle \widehat{P_{\alpha}} \rangle$$

where $\langle \widehat{P_{\alpha}} \rangle$ is an estimator of the mean value of the α -th operator defined as

$$\langle \widehat{P_{\alpha}} \rangle = \frac{1}{n_s} \sum_{i=1}^{n_s} X_{i,\alpha}$$

where n_s is the number of circuit evaluations (shots) and $X_{i,\alpha}$ is the measurement outcome of the i -th circuit evaluation. Since $\{X_{i,\alpha} : i = 1, \dots, n_s\}$ are independent and identically distributed (i.i.d.) random variables, the central limit theorem applies, and since n_s is of the order of magnitude 10^3 to 10^4 , the assumption that $\langle \widehat{P_{\alpha}} \rangle$ follows a normal distribution is reasonable. Taking a linear combination of $\langle \widehat{P_{\alpha}} \rangle$ to yield $\langle \widehat{H} \rangle$ preserves the Gaussian nature, as does further averaging over N independent trials $\{\langle \widehat{H} \rangle_j : j = 1, \dots, N\}$ to yield the ultimate estimator $\hat{E} \equiv \frac{1}{N} \sum_{j=1}^N \langle \widehat{H} \rangle_j$. The estimator of the variance of $\langle \widehat{H} \rangle$ is σ^2 , and so we take σ^2/N as (an estimator of) the variance of \hat{E} . Taking $N = \lceil \sigma^2/\epsilon^2 \rceil$ and assuming normality gives the greater than 68% probability that the energy estimate is within ϵ of the real value.

Again, see §V.A of Kandala et al.⁶ for the formula for σ^2 ; the variance must take into account correlations between estimators for different operators, since the same set of measurement outcomes may be used to evaluate $\widehat{P_\alpha}$ and $\widehat{P_\beta}$ ($\alpha \neq \beta$).

Even without assuming normality, we can use Chebyshev's inequality; the energy estimator \widehat{E} is a random variable with mean $\langle H \rangle$ and assume its variance is σ^2/N . Chebyshev's inequality gives

$$P\left(|\widehat{E} - \langle H \rangle| \geq \eta\sigma/\sqrt{N}\right) \leq \frac{1}{\eta^2}.$$

for any real $\eta > 0$. Taking $\eta > 1$ and $N = \eta^2\sigma^2/\epsilon^2$ guarantees that there is a nonzero probability that the estimator is within ϵ of the true mean.

Measurement error mitigation

Upon each VQE iteration, circuits are constructed and executed and measurements of these circuits are performed. To reduce the effect of measurement error, we employed an error mitigation technique implemented in Qiskit Ignis^{11,10}. The technique entails initially constructing a $2^n \times 2^n$ calibration matrix A , where n is the number of qubits in the device of interest, each row represents a basis state prepared in the device, and each column represents a basis state measured from the device after the rows' state preparation. For example, an element at row 6 and column 4 of a 32×32 -element matrix may represent the number of times a state prepared in $|00110\rangle$ was measured in the $|00100\rangle$ state during this calibration routine. We execute all such preparations and measurements on the quantum hardware as an initial calibration step to prepare the A matrix before any other experiments. Without any measurement or state preparation error, this matrix would equal the identity, as every row basis state would only be measured in its corresponding column basis state. We now want to approximate a transformation M from the measured matrix A to the identity:

$$\begin{aligned} I &= AM \\ M &= A^{-1} \end{aligned}$$

So, when we sample results from hardware, we simply multiply our row vector of measured basis state probabilities by A^{-1} to infer the measurement- mitigated vector. In practice, we use the pseudo-inverse or least squares optimization to find the inverse in case A has 0-valued eigenvalues and cannot be inverted. Note that this method scales exponentially in the number of basis states, but needs only be performed once as an initial device calibration step.

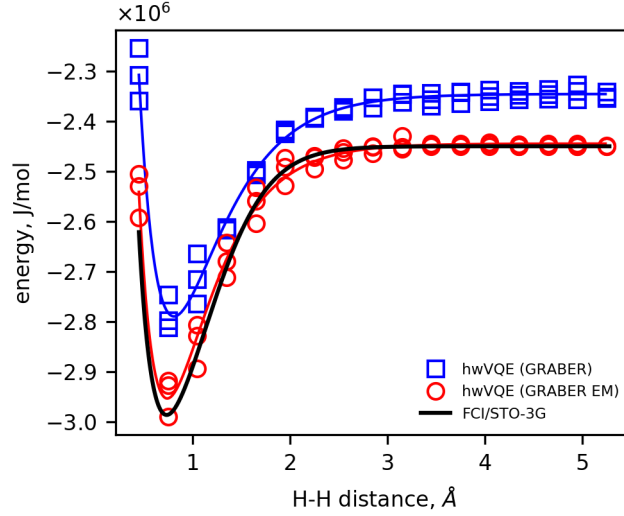


Figure 7: The solid line represents FCI/STO-3G calculations on a classical computer, every 0.01 Å from 0.45 to 5.3 Å. Squares and circles are calculations on the quantum computer with or without measurement error mitigation, hwVQE (GRABER EM) and hwVQE (GRABER), respectively.

Hardware

We tested the algorithms in several superconducting quantum hardware and simulation environments. We executed noisy simulations in Qiskit Aer, using default noise models constructed by Aer to represent the quantum devices which follow. We tested on a superconducting transmon quantum device with 5-qubits, called IBM Q Valencia. The topologies of the devices can be found in Figure 8. We interfaced with these devices through the Qiskit IBM Q Provider API utility, and executed 8192 shots per circuit evaluation.

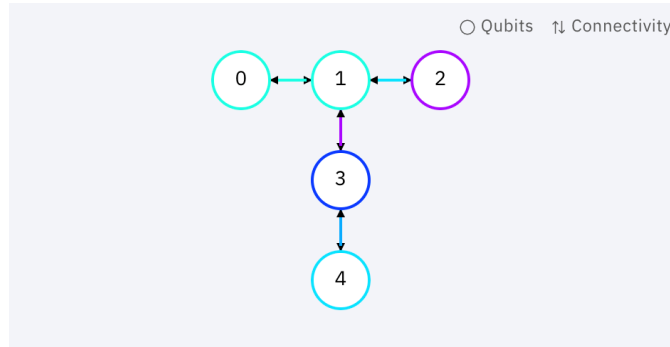


Figure 8: Topology of the 5-qubit IBM Q Valencia superconducting quantum device.

Acknowledgments

The authors thank Panagiotis Barkoutsos, Laurent White, and Gilad Ben-Shach for their comments and suggestions.

Author contributions

S.T.S. and S.M.H. contributed equally, developing the statistical mechanics approach, and classical optimizer, respectively. D.G. provided the measurement error mitigation procedure and advice on the hardware usage. T.P.G. provided the qubit-tapering procedure. S.M. provided the particle-hole mapping procedure. D.T. assisted in developing the code and provided theoretical guidance. S.R. assisted in developing the statistical mechanical approach.

Data availability

The datasets generated during and/or analysed during the current study are available from the corresponding author on reasonable request.

Ethics declarations

The authors declare no competing financial interests.

References

- [1] Richard P. Feynman. Simulating physics with computers. *International Journal of Theoretical Physics*, 21(6):467–488, 1982.
- [2] Daniel S. Abrams and Seth Lloyd. Simulation of many-body fermi systems on a universal quantum computer. *Physical Review Letters*, 79(13):2586–2589, 1997. doi: 10.1103/PhysRevLett.79.2586.
- [3] Ivan Kassal, James D. Whitfield, Alejandro Perdomo-Ortiz, Man-Hong Yung, and Aln Aspuru-Guzik. Simulating chemistry using quantum computers. *Annual Review of Physical Chemistry*, 62(1):185–207, 2011. doi: 10.1146/annurev-physchem-032210-103512.
- [4] Yudong Cao, Jonathan Romero, Jonathan P. Olson, Matthias Degroote, Peter D. Johnson, Mria Kieferov, Ian D. Kivlichan, Tim Menke, Borja Peropadre, Nicolas P. D. Sawaya, Sukin Sim, Libor Veis, and Aln Aspuru-Guzik. Quantum chemistry in the age of quantum computing. *Chemical Reviews*, 2019. ISSN 0009-2665. doi: 10.1021/acs.chemrev.8b00803.
- [5] Alberto Peruzzo, Jarrod McClean, Peter Shadbolt, Man-Hong Yung, Xiao-Qi Zhou, Peter J. Love, Aln Aspuru-Guzik, and Jeremy L. OBrien. A variational eigenvalue solver on a photonic quantum processor. *Nature Communications*, 5(1):4213, 2014.
- [6] Abhinav Kandala, Antonio Mezzacapo, Kristan Temme, Maika Takita, Markus Brink, Jerry M. Chow, and Jay M. Gambetta. Hardware-efficient variational quantum eigensolver for small molecules and quantum magnets. *Nature*, 549:242, 2017.
- [7] A. Aspuru-Guzik, A. D. Dutoi, P. J. Love, and M. Head-Gordon. Simulated quantum computation of molecular energies. *Science*, 309(5741):1704–7, 2005.
- [8] Panagiotis Kl Barkoutsos, Jerome F. Gonthier, Igor Sokolov, Nikolaj Moll, Gian Salis, Andreas Fuhrer, Marc Ganzhorn, Daniel J. Egger, Matthias Troyer, Antonio Mezzacapo, Stefan Filipp, and Ivano Tavernelli. Quantum algorithms for electronic structure calculations: Particle-hole hamiltonian and optimized wave-function expansions. *Physical Review A*, 98(2):022322, 2018.
- [9] S. Bravyi, J. M. Gambetta, A. Mezzacapo, and K. Temme. Tapering off qubits to simulate fermionic hamiltonians., 2017. URL <https://arxiv.org/abs/1701.08213>.

- [10] Qiskit ignis. <https://github.com/Qiskit/qiskit-ignis>. Accessed: 2019-12-30.
- [11] Héctor Abraham et al. Qiskit: An open-source framework for quantum computing, 2019.
- [12] Yangchao Shen, Xiang Zhang, Shuaining Zhang, Jing-Ning Zhang, Man-Hong Yung, and Kihwan Kim. Quantum implementation of the unitary coupled cluster for simulating molecular electronic structure. *Physical Review A*, 95(2):020501, 2017.
- [13] P. J O’Malley, R. Babbush, I. D Kivlichan, J. Romero, J. R McClean, R. Barends, J. Kelly, P. Roushan, A. Tranter, N. Ding, B. Campbell, Y. Chen, Z. Chen, B. Chiaro, A. Dunsworth, A. G Fowler, E. Jeffrey, E. Lucero, A. Megrant, J. Y Mutus, M. Neeley, C. Neill, C. Quintana, D. Sank, A. Vainsencher, J. Wenner, T. C White, P. V Coveney, P. J Love, H. Neven, A. Aspuru-Guzik, and J. M Martinis. Scalable quantum simulation of molecular energies. *Physical Review X*, 6(3):031007, 2016.
- [14] Cornelius Hempel, Christine Maier, Jonathan Romero, Jarrod McClean, Thomas Monz, Heng Shen, Petar Jurcevic, Ben P. Lanyon, Peter Love, Ryan Babbush, Aln Aspuru-Guzik, Rainer Blatt, and Christian F. Roos. Quantum chemistry calculations on a trapped-ion quantum simulator. *Physical Review X*, 8(3):031022, 2018.
- [15] Philip M. Morse. Diatomic molecules according to the wave mechanics. ii. vibrational levels. *Physical Review*, 34(1):57–64, 1929.
- [16] M. D Hutchings, J. B Hertzberg, Y. Liu, N. T Bromm, G. A Keefe, Markus Brink, Jerry M. Chow, and B. L T Plourde. Tunable superconducting qubits with flux-independent coherence. *Physical Review Applied*, 8(4):044003, 2017.
- [17] Clayton Gearhart. The rotational specific heat of molecular hydrogen in the old quantum theory. In *APS April Meeting, 2005*. URL <http://meetings.aps.org/link/BAPS.2005.APR.K11.1>.
- [18] David M. Dennison and Ralph Howard Fowler. A note on the specific heat of the hydrogen molecule. *Proceedings of the Royal Society of London. Series A, Containing Papers of a Mathematical and Physical Character*, 115(771):483–486, 1927.
- [19] M.W. Chase, Jr. *NIST-JANAF Thermochemical Tables, Fourth Edition*. J. Phys. Chem. Ref. Data, Monograph 9, 1998.
- [20] W. J. Hehre, R. F. Stewart, and J. A. Pople. Selfconsistent molecularorbital methods. i. use of gaussian expansions of slatertype atomic orbitals. *The Journal of Chemical Physics*, 51(6):2657–2664, 1969.
- [21] Nikolaj Moll, Panagiotis Barkoutsos, Lev S Bishop, Jerry M Chow, Andrew Cross, Daniel J Egger, Stefan Filipp, Andreas Fuhrer, Jay M Gambetta, Marc Ganzhorn, Abhinav Kandala, Antonio Mez-zacapo, Peter Mller, Walter Riess, Gian Salis, John Smolin, Ivano Tavernelli, and Kristan Temme. Quantum optimization using variational algorithms on near-term quantum devices. *Quantum Science and Technology*, 3(3):030503, jun 2018.
- [22] Yangchao Shen, Xiang Zhang, Shuaining Zhang, Jing-Ning Zhang, Man-Hong Yung, and Kihwan Kim. Quantum implementation of the unitary coupled cluster for simulating molecular electronic structure. *Phys. Rev. A*, 95:020501, Feb 2017. doi: 10.1103/PhysRevA.95.020501.
- [23] Gavin E. Crooks. Gradients of parameterized quantum gates using the parameter-shift rule and gate decomposition. *arXiv preprint arXiv:1905.13311*, 2019.
- [24] Dimitri P. Bertsekas and John N. Tsitsiklis. Gradient convergence in gradient methods with errors. *SIAM Journal on Optimization*, 10(3):627–642, 2000.

- [25] J. I Colless, V. V Ramasesh, D. Dahlen, M. S Blok, M. E Kimchi-Schwartz, J. R McClean, J. Carter, W. A de Jong, and I. Siddiqi. Computation of molecular spectra on a quantum processor with an error-resilient algorithm. *Physical Review X*, 8(1):011021, 2018.
- [26] Raffaele Santagati, Jianwei Wang, Antonio A. Gentile, Stefano Paesani, Nathan Wiebe, Jarrod R. McClean, Sam Morley-Short, Peter J. Shadbolt, Damien Bonneau, Joshua W. Silverstone, David P. Tew, Xiaoqi Zhou, Jeremy L. OBrien, and Mark G. Thompson. Witnessing eigenstates for quantum simulation of hamiltonian spectra. 4(1):9646, 2018.
- [27] Robert M. Parrish, Lori A. Burns, Daniel G. A. Smith, Andrew C. Simmonett, A. Eugene DePrince, Edward G. Hohenstein, Uur Bozkaya, Alexander Yu Sokolov, Roberto Di Remigio, Ryan M. Richard, Jrme F. Gonthier, Andrew M. James, Harley R. McAlexander, Ashutosh Kumar, Masaaki Saitow, Xiao Wang, Benjamin P. Pritchard, Prakash Verma, Henry F. Schaefer, Konrad Patkowski, Rollin A. King, Edward F. Valeev, Francesco A. Evangelista, Justin M. Turney, T. Daniel Crawford, and C. David Sherrill. Psi4 1.1: An open-source electronic structure program emphasizing automation, advanced libraries, and interoperability. *Journal of Chemical Theory and Computation*, 13(7):3185–3197, 2017.
- [28] Donald A. McQuarrie. *Statistical Mechanics*. University Science Books, Sausalito, CA, 2000.
- [29] G. H. Wannier. *Statistical Physics*. John Wiley and Sons, Inc., New York, NY, 1966.
- [30] R. E. Cornish and E. D. Eastman. The specific heat of hydrogen gas at low temperatures from the velocity of sound; and a precision method of measuring the frequency of an oscillating circuit. *Journal of the American Chemical Society*, 50(3):627–652, 1928.
- [31] A. Popovas and U. G. Partition functions. 595:A130, 2016.
- [32] Q. M. Sun, T. C. Berkelbach, N. S. Blunt, G. H. Booth, S. Guo, Z. D. Li, J. Z. Liu, J. D. McClain, E. R. Sayfutyarova, S. Sharma, S. Wouters, and G. K. L. Chan. Pyscf: the python-based simulations of chemistry framework. *Wiley Interdisciplinary Reviews-Computational Molecular Science*, 8(1):e1340, 2018.
- [33] S. Bravyi and A. Kitaev. Fermionic quantum computation. *Ann. of Phys.*, 298(1):210, 2002.
- [34] Jacob T. Seeley, Martin J. Richard, and Peter J. Love. The bravyi-kitaev transformation for quantum computation of electronic structure. *The Journal of Chemical Physics*, 137(22):224109, 2012.
- [35] P. Jordan and E. Wigner. Über das paulische Äquivalenzverbot. *Z. Phys*, 47(9-10):631, 1928.
- [36] K. Setia, R. Chen, J. E. Rice, A. Mezzacapo, M. Pistoia, and J. Whitfield. Reducing qubit requirements for quantum simulation using molecular point group symmetries., 2019. URL <https://arxiv.org/abs/1910.14644>.